Heliyon 10 (2024) e40776

Contents lists available at ScienceDirect

Heliyon

journal homepage: www.cell.com/heliyon

Research article

Investigation of structural, optical, antibacterial, and dielectric properties of sol-gel and biosynthesized TiO_2 nanoparticles

Abdullah Al Moyeen [a], Raiyana Mashfiqua Mahmud [a], Durjoy Datta Mazumder [b], Sondip Ghosh [a], Orchi Datta [a], Anik Molla [a], M. Esmotara Begum [a,*]

[a] Department of Glass & Ceramic Engineering, Rajshahi University of Engineering & Technology (RUET), Rajshahi-6204, Bangladesh
[b] Department of Materials Science & Engineering, Rajshahi University of Engineering & Technology (RUET), Rajshahi-6204, Bangladesh

ARTICLE INFO

Keywords:
Sol-gel
Biosynthesis
Allium sativum
Band gap
Antibacterial activity
Dielectric properties

ABSTRACT

This study explored the structural, optical, antibacterial, and dielectric properties of TiO_2 nanoparticles synthesized using two distinct approaches: sol-gel and biosynthesis. Density functional tight binding (DFTB+) and density functional theory (DFT) calculations were employed alongside experimental techniques to gain a comprehensive understanding of the electronic-property relationships. *Allium sativum* peel extract was utilized for the biosynthesis method. X-ray diffraction (XRD) affirmed the anatase phase formation for both nanoparticles. Rietveld technique was employed for a detailed structural analysis. The FESEM analysis revealed the diminutive particle size of TiO_2 nanoparticles with a comparable size distribution for both variants. However, the biosynthesized variant exhibited smaller average particle size (26.74 nm) than the sol-gel variant (32.22 nm). Optical studies showed an absorption redshift for the biosynthesized variant (352 nm) relative to the sol-gel variant (347 nm). The band gap energy is higher for the sol-gel variant (3.17 eV) compared to the biosynthesized variant (3.02 eV). The biosynthesized nanoparticles showed strong antibacterial activity, with inhibition zones of 15 mm against *E. coli* and *S. flexneri* bacteria. Dielectric analysis revealed that the sol-gel synthesized nanoparticles exhibited a higher dielectric permittivity of 27.80 and a lower dielectric loss of 0.37 at 1 kHz, compared to the biosynthesized nanoparticles, which showed a dielectric permittivity of 19.48 and a dielectric loss of 0.69.

1. Introduction

Nanoparticles, sizes in the range of 100 nm exhibit significant changes in optical, magnetic, and electrical properties compared to their bulk counterparts. These distinct properties of nanoparticles are driven by quantum confinement effects, a high surface-to-volume ratio, minimal gravitational forces, and dominating electromagnetic forces [1,2]. These remarkable properties of nanoparticles have revolutionized numerous fields, including nanotechnology, biology, optics, photocatalysis, sensing, and electronic systems [3]. Among different nanoparticles, metal oxides like ZnO, CuO, TiO_2, MgO etc., have demonstrated their potential in diverse applications. Among these, TiO_2 stands out for its versatility, non-toxicity, and exceptional electrical properties, finding its applications in the fields of environmental remediation, photovoltaics, energy storage devices, self-cleaning surfaces, and biomedical devices.

TiO_2 exists in three distinct crystalline phases (anatase, brookite, and rutile), offers a range of properties that can be tailored for

* Corresponding author.
E-mail addresses: abdullah264253@gmail.com (A.A. Moyeen), meb@gce.ruet.ac.bd (M.E. Begum).

https://doi.org/10.1016/j.heliyon.2024.e40776
Received 12 September 2024; Received in revised form 2 November 2024; Accepted 27 November 2024
Available online 28 November 2024

specific applications [4]. Notably, anatase TiO_2 nanoparticles (NPs) possess excellent optical and dielectric properties along with biocompatibility, and high thermal stability [5]. These attributes have led to their widespread use in photocatalysis, dye-sensitized solar cells (DSSCs), lithium-ion batteries, optoelectronic devices, hydrogen peroxide (H_2O_2) reduction, and solar cells [6–8]. However, the selection of synthesis methods for TiO_2 nanoparticles plays a crucial role in determining their crystalline phases, which in turn affects their structural, optical, antibacterial, and electrical characteristics [9]. In recent years, a variety of synthesis methods have been developed to tailor the structure and properties of TiO_2 nanostructures, including the sol-gel process, solvothermal synthesis, electrodeposition, direct oxidation, chemical vapor deposition, hydrothermal techniques, and biosynthesis [10–14]. Table 1 summarizes the influence of various synthesis approaches and calcination conditions on the size and optical properties of TiO_2 NPs.

It is noteworthy that, most of the synthesis techniques require a controlled atmosphere, expensive instrumentation, and the use of chemical components to reduce and control nanoparticle sizes. Among these methods, the sol-gel process stands out for its simplicity and ease of handling, yet it can produce TiO_2 NPs with excellent photocatalytic activity, high crystalline quality, well-controlled particle size and shape [26]. The conventional sol-gel method involves the hydrolysis and polycondensation of metal alkoxide, leading to the formation of oxopolymers, which are then converted into an oxide network. The structural and characteristic properties of the resulting metal oxides are significantly affected by the rates of hydrolysis and polycondensation during synthesis [27]. This process often requires the use of additional chemicals to control particle sizes, which are eventually released into the atmosphere.

Another promising approach, the biosynthesis method, has gained wide acceptance due to its ability to eliminate the toxic effects associated with various traditional chemical synthesis methods [28]. Utilizing plant elements for nanoparticle synthesis is particularly desirable because it is a one-step green reduction method that requires less energy, resulting in eco-friendly nanoparticles with diverse properties, high stability, and suitable dimensions. The use of plant extracts in the biosynthesis of TiO_2 nanoparticles has emerged as a promising alternative due to its environmentally friendly and cost-effective nature. Biologically synthesized TiO_2 NPs exhibit not only excellent antibacterial activity but also diverse biological properties such as anti-inflammatory, antifungal, and antimicrobial functionalities. Additionally, the photo-semiconductor capabilities of these nanoparticles enhance their biological activity, making them highly effective in various applications [29]. Several plant extracts have been explored for the synthesis of TiO_2 NPs, including *Acorus calamus* leaf, Aloe vera leaf, *Jatropha curcas* L., Lemon peel, and more [15,18,25,30]. In addition, Garlic peels (*Allium sativum*) hold immense promise for eco-friendly synthesis of TiO_2 NPs. It is recognized for their exceptional physiological activity [31]. The presence of bioactive components such as phenolics, flavonoids, alliin, and allicin in garlic peel extract contributes to its high ability to scavenge free radical [32]. Although commonly seen as waste, the peels of *Allium sativum* can be repurposed as a reducing agent, making their use a sustainable approach in nanoparticle production.

In this study, the authors aimed to synthesize TiO_2 NPs using two methods: a traditional sol-gel approach and a novel biosynthesis technique utilizing garlic peel extract. A detailed comparison was then conducted on the TiO_2 NPs, in terms of their structural, optical, antibacterial, and dielectric properties. The study integrated experimental techniques with DFTB+ and DFT calculations to provide an in-depth analysis of the relationships between electronic properties and nanoparticle characteristics.

2. Computational and experimental methods

2.1. Calculation model and method

In the present work, density functional theory and density functional tight binding methods were used. In the context of the implementation of DFT, Schrödinger equation (Eqn. (1)) remains all-important of this calculation.

Table 1
Influence of different synthesis techniques and calcination conditions on TiO_2 NPs size and optical properties.

Methods	Calcination	Particle Size	Absorption Maxima	Band Gap	Ref.
Biosynthesis *Acorus calamus* leaf	600 °C (3 h)	11–30 nm	355 nm	3.20	[15]
Sol-gel	400 °C (3 h)	~13 nm	432 nm	2.90	[16]
Hydrothermal	500 °C (2 h)	32–48 nm	385 nm	–	[17]
Biosynthesis Lemon peel	500 °C (2 h)	80–140 nm	325 nm	3.08	[18]
Biosynthesis Gum Kondagogu	500 °C (4 h)	8–13 nm	330 nm	3.13	[19]
Simple precipitation	500 °C (1 h)	7–21 nm	475 nm	3.30	[20]
Biosynthesis *Acorus calamus* leaf	600 °C (3 h)	11–30 nm	360 nm	3.29	[21]
Biosynthesis *Citrus Limetta*	550 °C (2 h)	80–100 nm	300 nm	3.22	[22]
Solvothermal	200 °C (2 h)	~13.4 nm	381 nm	3.20	[23]
Sol-gel	450 °C (3 h)	≥80 nm	350 nm	3.20	[24]
Biosynthesis Aloe vera leaf	500 °C (5 h)	10–80 nm	344 nm	3.19	[25]
Sol-gel	500 °C (3 h)	20–45 nm	347 nm	3.17	This work
Biosynthesis *Allium sativum* peel	500 °C (3 h)	15–35 nm	352 nm	3.02	This work

$$\widehat{H}\Psi = E\Psi \tag{1}$$

where E represents the energy of the system, $\widehat{H}$ is the Hamiltonian operator, and Ψ denotes the wavefunction. To simplify this equation, the Born–Oppenheimer approximation is often applied. The methods of the DFT, based upon the Kohn-Sham theorem, make it possible to solve problems concerned with molecular and solid material electronics. It adeptly transforms the daunting many-electron problem into a more manageable single-electron framework. This is achieved through the Hohenberg–Kohn theorems, which state that the ground-state properties of a system are determined by its electron density, $\rho(r)$. The Kohn–Sham equation (Eqn. (2)) then permit the computation of the total energy $(E_v[\rho])$ via a non-interacting reference system.

$$E_v[\rho] = T_s[\rho] + E_{xc}[\rho] + \int \rho(r) v_{ext}(r)\, dr + \frac{1}{2}\int \frac{\rho(r)\rho(r')}{|r-r'|}\, dr\, dr' \tag{2}$$

In this expression, $T_s[\rho]$ signifies the kinetic energy of the non-interacting electrons, v_{ext} represents the external potential, and E_{xc} denotes the exchange-correlation energy. To approximate the exchange-correlation energy, methodologies such as the Generalized Gradient Approximation (GGA) and the Local Density Approximation (LDA) were employed. Specifically, for GGA, the Perdew-Burke-Ernzerhof (PBE) functional defines the E_{xc} as Eqn. (3).

$$E_{XC}^{GGA}[\rho] = \int \rho(r)\epsilon_{XC}^{hom}(\rho(r), \nabla\rho(r)\,)\, dr \tag{3}$$

Conversely, LDA presupposes that the exchange-correlation energy density at any given point is determined solely by the local electron density $(\rho(r))$, as shown in Eqn. (4).

$$E_{XC}^{LDA}[\rho] = \int \rho(r)\epsilon_{XC}^{hom}(\rho(r))\, dr \tag{4}$$

The Ceperley-Alder/Perdew-Zunger (CA-PZ) functional represents a specific LDA formulation. Collectively, these methods constitute the foundation of DFT, facilitating the efficient exploration of the electronic structures inherent in complex systems [33].

In our alternative computational approach, we employed DFTB+ within Materials Studio, which is an efficient implementation of the Density Functional based Tight Binding (DFTB) method. DFTB is a streamlined version of DFT, where the total energy of a system is expanded using a Taylor series derived from Kohn-Sham density functional theory. The electron density $(\rho(r))$ is expressed as the sum of a reference density $(\rho_0(r))$ and a small fluctuation $(\delta\rho(r))$, as shown in Eqn. (5).

$$\rho(r) = \rho_0(r) + \delta\rho(r) \tag{5}$$

The total energy $(E[\rho])$ in DFTB is then expanded as Eqn. (6).

$$E[\rho] = E_0[\rho_0] + E_1[\rho_0, \delta\rho] + E_2\left[\rho_0, (\delta\rho)^2\right] + E_3\left[\rho_0, (\delta\rho)^3\right] \tag{6}$$

In this expansion, E_0 and E_1 form the basic DFTB (1) model, which is the simplest version of DFTB. The term E_2 incorporates second-order corrections, defining the DFTB2 model, while E_3 adds third-order corrections, leading to the more accurate DFTB3 model. The different DFTB models have reasonably clear areas of application, with each level (DFTB (1), DFTB2, and DFTB3) balancing computational efficiency and precision, making DFTB highly effective for large-scale materials simulations due to its significant speed advantage over DFT [34]. This makes DFTB ideal for systems involving weak interactions, such as Van der Waals complexes [35].

In this study, Geometry optimization of the structure was carried out using the DFTB+ approach within the Materials Studio with the "Smart" technique, 0.05 kcal/mol energy convergence, and 0.5 kcal/mol/Å force convergence over a maximum of 500 cycles. To solve the Schrödinger equation for bonded electrons, the 'tiorg' Slater-Koster library was used for SCC calculations, with a tale of 1×10^{-5} and 50 maximum iterations. DFT calculations as a comparison were implemented with Materials Studio CASTEP software using the LDA and the CA-PZ functional and Koelling-Harmon relativistic treatment. Pseudopotentials were in reciprocal disposed space, and 300 eV plane wave cut-off, total electrons 48, non-spin-polarized conditions, and 24 bands. Energy minimization converged with a 0.2×10^{-5} eV tolerance, total energy per atom, and 0.5×10^{-6} eV eigen energy over a maximum of 100 SCF cycles, with the Pulay scheme for density mixing. Band structure calculations included 46 bands per k-point, with a 0.1×10^{-4} eV convergence tolerance. In addition, Perdew-Burke-Ernzerhof (PBE)/Generalized Gradient Approximation (GGA) functional DFT was calculated with similar conditions 300 eV cut-off, 48 electrons, non-spin-polarized, 24 bands, and Monkhorst-Pack grid size $4 \times 4 \times 5$ with 26 k-points. For the computational analysis of dielectric properties, we employed DFT calculations, utilizing the Generalized Gradient Approximation with the Perdew-Burke-Ernzerhof functional. The computations were performed along the [1 0 0] polarization axis, with a scissors operator of 0 eV applied. An instrumental smearing of 0.5 eV was used to account for broadening effects, while the plasma frequency was set to 0 eV.

2.2. Experimental

2.2.1. Synthesis of TiO_2 NPs by sol-gel method

For the preparation of TiO_2 NPs by the sol-gel process, 80 mL ethanol was mixed with 10 mL deionized water under constant stirring using a magnetic stirrer. Then 5 mL titanium isopropoxide (TTIP) was added by dropwise to the above-mixed solution under

constant stirring and followed by a 15 h stirring period. Subsequently, the resulting gel was dried in the hot-air oven at a temperature of 80 °C for 8 h. Further, the calcination was performed for 3 h at 500 °C and the prepared sample was named 'TSol'.

2.2.2. Synthesis of TiO_2 NPs by biosynthesis method

The outer peels of *Allium sativum* were cleaned with tap and deionized water, cut into small pieces, and mixed with 100 mL of deionized water. This mixture was boiled at 80 °C for 30 min to extract bioactive compounds. After cooling to room temperature, the extract was filtered using Whatman No. 1 filter paper to remove impurities. The extract was then refrigerated for further use.

A 0.1 M solution of TTIP in 80 mL of deionized water was prepared. Then, 40 mL of *Allium sativum* peel extract was added, and the mixture was stirred at 600 rpm for 3 h at 60 °C, with pH controlled using a few drops of NH_3 (aq.). The solution was kept for 24 h to complete gelation and aging. Afterward, the mixture was centrifuged and rinsed with ethanol and deionized water. The TiO_2 NPs were dried at 80 °C for 8 h and then calcined at 500 °C for 3 h. The prepared sample was named 'TBio'.

2.2.3. Pellet preparation

The TiO_2 NPs were formed into pellets for electrical characterization. Each nanoparticle sample weighing 1 g was mixed with a polyvinyl alcohol binder and compacted into disk-shaped pellets with a diameter of 12 mm under a pressure of 2.5 tons. Subsequently, the pellets underwent sintering in an air environment at 750 °C.

2.2.4. Characterization

Crystallographic analysis of TiO_2 NPs was performed using a SHIMADZU LabX XRD-6100 (Japan) instrument. The X-ray diffraction (XRD) data was analyzed using the FullProf software via Rietveld refinement. Field emission scanning electron microscopy (FESEM) was employed to investigate the surface morphology of the TiO_2 NPs using a JEOL JSM-7600F (Germany) instrument. ImageJ software was then utilized to assess the avg. particle size and distribution from the FESEM images.

The UV–vis absorption spectrum of TiO_2 NPs was measured using a Shimadzu UV-2600i (Japan) spectrophotometer over wavelengths from 250 to 800 nm. An ethanol suspension of the nanoparticles was utilized for the analysis.

The antibacterial activity of the synthesized TiO_2 NPs was evaluated using the agar well diffusion method against four bacterial strains: gram-positive *Staphylococcus aureus* (ATCC25923), and gram-negative *Escherichia coli* (ATCC25922), *Pseudomonas aeruginosa* (ATCC27853), and *Shigella flexneri* (clinical isolate). Fresh bacterial cultures were uniformly spread on agar plates. Paper discs

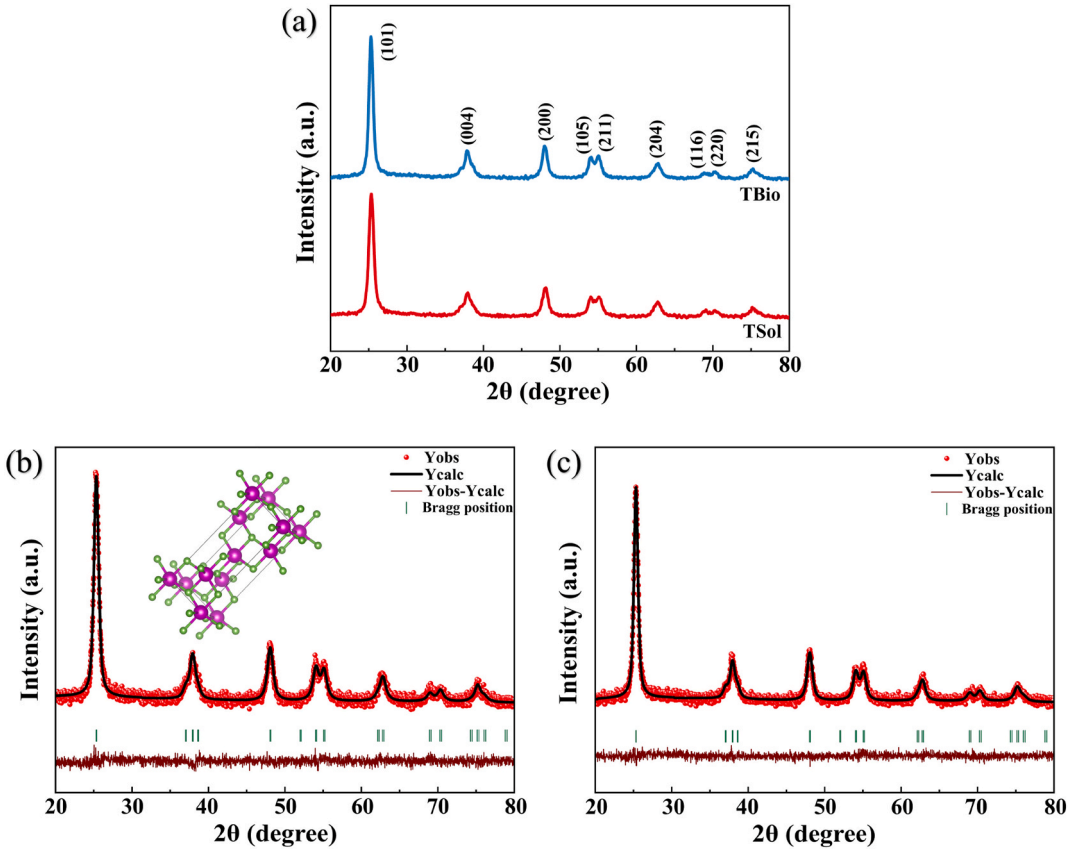

Fig. 1. (a) XRD patterns of TiO_2 NPs and Rietveld refined pattern of (b) TSol and (c) TBio.

containing TiO_2 NPs at concentrations of 100, 200, and 300 μg/mL were placed on the agar surface and incubated for 24 h at 30 °C. The zones of inhibition, represented as circular areas around the discs where bacterial growth was suppressed, were measured in millimeters.

The dielectric measurements of the synthesized TiO_2 nanoparticle pellets were investigated using the conventional parallel plate capacitor method. Measurements were performed in the frequency range of 40 Hz to 10 kHz with an Agilent 4294A Precision Impedance Analyzer (USA).

3. Results and discussion

3.1. Structural characteristics

Fig. 1a presents the XRD patterns of TSol and TBio samples acquired in 2θ range of 20–80°. According to JCPDS card No. 01-084-1286, the intense peaks of TiO_2 NPs are identified along the (101), (004), (200), (105), (211), (204), (116), (220), and (215) planes. Table 2 compares the XRD peak positions (2θ) of TSol and TBio NPs with the standard values. The indexed planes confirm the pure tetragonal anatase phase of TiO_2, characterized by octahedral and trigonal planar coordination geometry [16]. Interestingly, the TBio sample have higher intensity peaks compared to the TSol sample. This observation might be attributed to the existence of polyphenolic compounds within the plant extract used for biosynthesis [17]. These biomolecules can potentially influence the crystallization process, leading to the formation of NPs with improved crystallinity.

For a more quantitative analysis of the crystallographic structure, the obtained XRD data were subjected to Rietveld refinement using the FullProf software. A Pseudo-Voigt fitting function was employed. The final refined parameters, including lattice parameters, cell volume, and profile R-factors, are summarized in Table 3. The good agreement between the calculated and observed XRD patterns (Fig. 1b and c) suggests a high-quality fit and supports the presence of a pure anatase phase. Furthermore, the crystallographic structure of the anatase TiO_2 NPs was visualized using the VESTA software (inset of Fig. 1b, violet and green spheres represent titanium and oxygen atoms, respectively).

The crystallite size of the TiO_2 NPs was determined using Scherrer's equation based on the prominent diffraction peak corresponding to the (101) plane. Scherrer's equation is expressed as: $d = 0.89\lambda/\beta\cos\theta$, where d represents the crystallite size (nm), λ is the X-ray wavelength (nm), β is the full width at half maximum (FWHM), and θ is the Bragg diffraction angle [36]. The estimated crystallite sizes were ~9.54 and ~11.14 nm for the TSol and TBio samples, respectively. These values are quite comparable with the reported literature [37,38]. Furthermore, the observed peak broadening in the XRD pattern of the TSol sample also support the presence of a smaller crystallite size compared to TBio [16].

The crystallinity of the TiO_2 NPs was further quantified using the XRD data. This analysis involved calculating the percentage contribution of the crystalline and amorphous phases within the samples. By this method, the crystallinity of the sol-gel synthesized TiO_2 NPs was determined to be 75.76 %, while the biosynthesized NPs exhibited a higher crystallinity of 78.56 %. All the crystallographic parameters are presented in Table 3.

3.2. Morphological analysis

Fig. 2 displays the FESEM micrographs of TSol and TBio nanoparticles. The FESEM observations indicate that both samples exhibited predominantly spherical nanoparticles. Interestingly, the biosynthesized TiO_2 NPs displayed a more uniform size distribution compared to the TSol NPs. The sol-gel synthesized nanoparticles showed a tendency to form irregular, aggregated structures, possibly due to the rapid hydrolysis and condensation reactions during the synthesis process. In contrast, the TBio NPs appeared clearer, lighter, and less prone to agglomeration. This suggests that the garlic peel extract acted as a stabilizing agent during the synthesis process, influencing the growth and dispersion of the nanoparticles.

The inset histograms in Fig. 2a, b depict the particle size distribution for each sample. The majority of particles in the TSol sample fall within the range of 20–45 nm, while the TBio sample exhibits a narrower size distribution with particles ranging from 15 to 35 nm. The avg. particle size was calculated to be 32.22 nm for TSol and 26.74 nm for TBio. This confirms the effectiveness of the garlic peel extract in reducing the particle size of the biosynthesized TiO_2 NPs.

Table 2
Shows comparison of XRD data of TiO_2 NPs with standard value.

Miller Plane (hkl)	JCPDS Card No: 01-084-1286 (2θ)	TSol (2θ)	TBio (2θ)
101	25.32	25.34	25.30
004	37.84	37.93	37.94
200	48.07	48.09	48.02
105	53.95	54.03	54.02
211	55.10	55.11	55.05
204	62.75	62.76	62.75
116	68.84	69.04	69.04
220	70.34	70.30	70.29
215	75.12	75.30	75.27

Table 3
Crystallographic parameters of TSol and TBio NPs.

Crystallographic parameters		TSol	TBio
Lattice parameters	a = b	3.785 Å	3.787 Å
	c	9.487 Å	9.484 Å
Cell Volume		135.886 $Å^3$	135.980 $Å^3$
R-factors	R_p	3.37	3.41
	R_{wp}	4.26	4.35
	R_{exp}	3.99	4.05
	Rf-factor	1.53	2.71
	Bragg R-factor	2.23	4.07
GOF		1.1	1.1
X-ray density		4.160 gcm^{-3}	4.044 gcm^{-3}
FWHM		0.8377	0.7157
Crystallite size	For (101) plane	9.536 nm	11.139 nm
Crystallinity		75.76 %	78.56 %

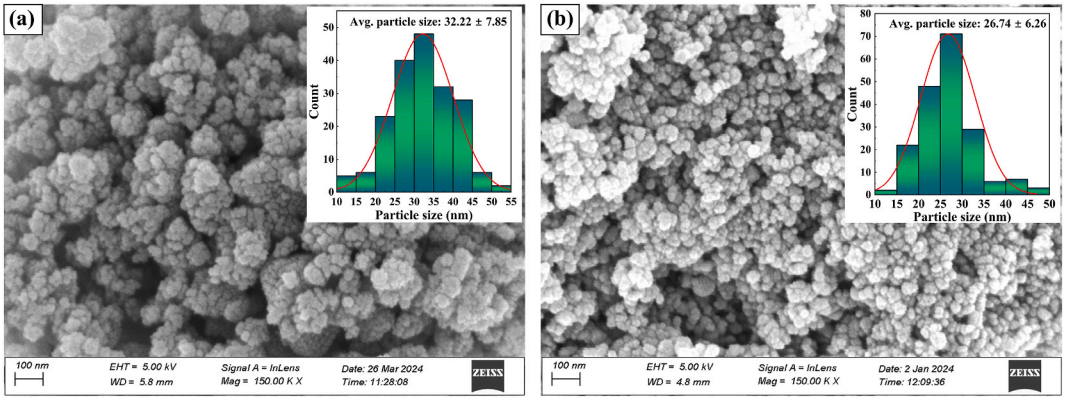

Fig. 2. FESEM image of (a) TSol and (b) TBio and inset showing particle size distribution.

3.3. Optical properties

Fig. 3a shows the absorption spectra of TiO_2 NPs fabricated using sol-gel and biosynthesis methods. Understanding optical properties is crucial for photocatalysis study, as they determine the light absorption efficiency of the material during the photocatalysis process [22]. The UV–visible absorption profile of the synthesized nanoparticles spans from 250 nm to 800 nm. Both types of

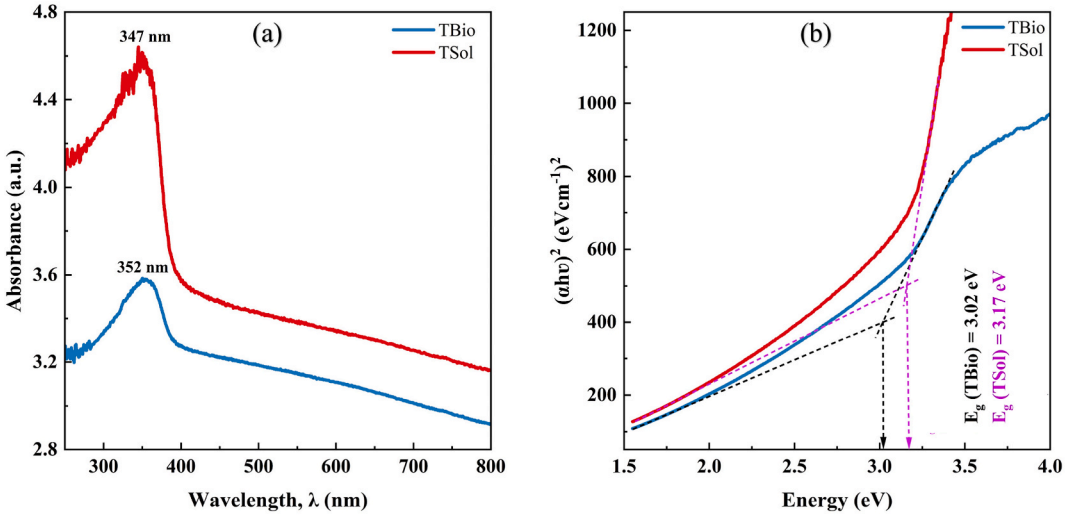

Fig. 3. (a) UV–vis absorption spectrum and (b) the Tauc plot of TiO_2 NPs.

nanoparticles exhibited a characteristic absorption spectrum with a single broad peak in the UV region. The observed absorption peak originates from the excitation of electrons from the valence band of the TiO_2 NPs to the conduction band. The absorption maxima (λ_{max}) for TSol and TBio NPs were found to be 347 nm and 352 nm, respectively, further confirming the presence of TiO_2 [25]. The observed slight red shift in the absorption peak of TBio NPs compared to TSol NPs could be attributed to variations in particle size and configuration.

The direct band gap energy (E_g) of the TiO_2 NPs was evaluated by employing the Tauc relation (Fig. 3b) [39]. The E_g of TSol NPs was found to be 3.17 eV, which is higher than that of TBio NPs (3.02 eV). The Tauc plot was employed here to more accurately determine the band gap energy, as broadened absorption peaks can sometimes obscure precise absorption values. The E_g values reported by Alhalili et al. [25] (3.19 eV with an absorption peak at 344 nm) and Zedek et al. [40] (3.02 eV with a peak near 350 nm) are quite similar to those observed in our samples. Furthermore, the difference in E_g between TSol and TBio NPs can be primarily explained by the quantum confinement effect [41]. According to this, the confinement of electrons and holes within the smaller crystallites of TSol NPs results in discrete energy levels and a consequent widening of the band gap. Moreover, the reduced band gap of TBio NPs could be ascribed to the existence of localized gap states induced by Ti^{3+} ions [42,43]. Additionally, oxygen vacancies within the crystal lattice might also contribute to the reduction in band gap energy, potentially enhancing their photocatalytic activity [42]. Since a narrower band gap corresponds to improved light absorption in the visible region, the TBio NPs with their lower E_g value (3.02 eV) are expected to demonstrate improved photocatalytic activity compared to the TSol NPs (3.17 eV) [44].

3.3.1. *Computational analysis of the band gap*

In the present work, we used a variety of computational approaches to study the band gap of TiO_2 NPs. We compared the obtained results with experimental findings to determine their validity in this section. The band gap was experimentally determined based on the UV–vis spectroscopy to be 3.17 eV for TSol NPs, and 3.02 eV for TBio NPs. From the DFTB+ simulations the band gap was determined to be 3.189 eV (See Fig. 4a), demonstrating excellent agreement with the experimental band gap of TSol NPs as well as TBio NPs. Conversely, DFT calculations using various functionals produced significantly lower values. For DFT calculations, different computational settings were employed. Using the GGA/PBE functional with a $4 \times 4 \times 5$ k-point grid and a plane wave cutoff of 300 eV, the convergence process yielded total energies of −429.2137 eV for oxygen after 23 iterations and −1596.0330 eV for titanium after 32 iterations. The resulting band gap was 2.091 eV (See Fig. 4b). For Local Density Approximation (LDA) with CA-PZ functional, similar parameters were used. Convergence was attained after 24 iterations for oxygen, resulting in a total energy of −428.3332 eV, and after 32 iterations for titanium, yielding a total energy of −1594.8364 eV. The band gap was 2.048 eV, as depicted in Fig. 4c. Both studies demonstrated high computational efficiency, with the GGA/PBE method obtaining an impressive parallel efficiency of 89 % for G-vector and k-point parallelization. Similarly, the LDA/CA-PZ method achieved a commendable efficiency of 87 %, highlighting the effective distribution of data by G-vector (6-way) and k-point (2-way).

Additionally, the density of states (DOS) calculations provide crucial insights into the electronic behavior of TiO_2. Fig. 5 illustrates the distribution of electronic states near energy levels in the DOS, essential for understanding the material's conductivity and optical

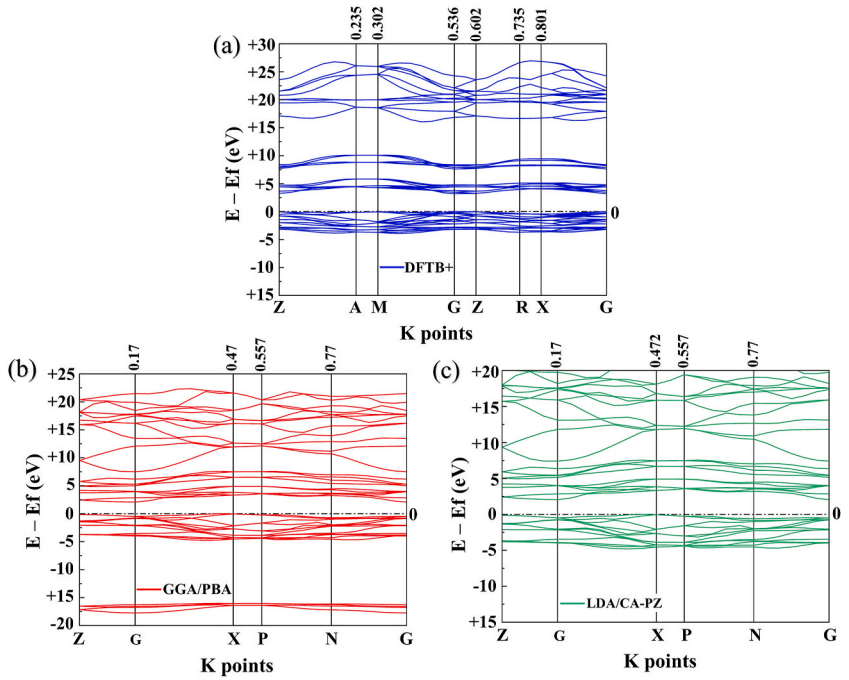

Fig. 4. Bandgap visualization of TiO_2 calculated by (a) DFTB+, (b) GGA/PBE, and (c) LDA/CA-PZ functional.

properties.

In summary, DFTB+ outperformed other methods, accurately predicting the band gap of TiO_2 (3.189 eV) close to experimental values. On the other hand, DFT techniques that employed GGA/PBE and LDE/CA-PZ functionals showed a notable underestimation of the band gap, with respective values of 2.091 eV and 2.048 eV. These results highlight the limitations of GGA/PBE and LDA-based functionals in accurately predicting the band gap of TiO_2 and underscores the superiority of DFTB+ for investigating the electronic properties of TiO_2 and similar materials.

3.4. Antibacterial activity

The antibacterial efficacy of TiO_2-based materials is attributed primarily to the generation of reactive oxygen species (ROS) [45,46]. These ROS, including hydroxyl radicals as well as superoxide anions, are extremely reactive and can directly damage bacterial cell walls [47]. The resultant damage to cellular components such as lipids, DNA, and proteins ultimately results in the loss of cellular functions and cell death [48,49]. Fig. 6 illustrates the antibacterial activity mechanism of TiO_2 NPs.

In this research, the antibacterial properties of TiO_2 NPs synthesized via sol-gel and biosynthesis methods were evaluated against both gram-positive and gram-negative bacteria. Fig. 7 illustrates the antibacterial efficacy of both TSol and TBio NPs against *Escherichia coli*, *Staphylococcus aureus*, *Pseudomonas aeruginosa*, and *Shigella flexneri*. The histogram depicting the zones of inhibition (ZOI) is presented in Fig. 8. The cell walls of gram-positive bacteria possess a thick peptidoglycan layer, whereas gram-negative bacteria have a thin peptidoglycan layer. Microbial pathogens can cause various diseases in living organisms. The maximum ZOI observed for TSol NPs against the gram-negative bacteria *E. coli*, *P. aeruginosa*, and *S. flexneri* were 12 mm, 14 mm, and 10 mm, respectively. For the gram-positive bacterium *S. aureus*, the ZOI was 12 mm. Interestingly, *P. aeruginosa* demonstrated the most significant zone of inhibition among the bacteria tested for TSol NPs.

The TBio NPs, however, demonstrated overall higher antibacterial activity compared to TSol. This enhanced efficacy can likely be attributed to their smaller particle size and higher surface area than TSol NPs, which aligns with observations reported by Krishna R. Raghupathi [50], suggesting that the antibacterial activity of nanoparticles is a size-dependent property that increases with particle size reduction. The maximum ZOI for TBio NPs against *E. coli*, *P. aeruginosa*, and *S. flexneri* were 15 mm, 12 mm, and 15 mm, respectively. The bacteria *S. aureus* showed similar susceptibility to TSol NPs (12 mm). Notably, *E. coli* and *S. flexneri* displayed the highest susceptibility to TBio NPs.

3.5. Dielectric properties

The dielectric properties of a material are closely linked to its electro-optic response. In the microelectronics industry, materials with low dielectric constants are particularly sought after for applications as interlayer dielectrics [51]. In this study, the frequency dependence of the dielectric constant (ε') and the loss tangent ($\tan\delta$) were measured for pelletized TiO_2 nanoparticle samples. The

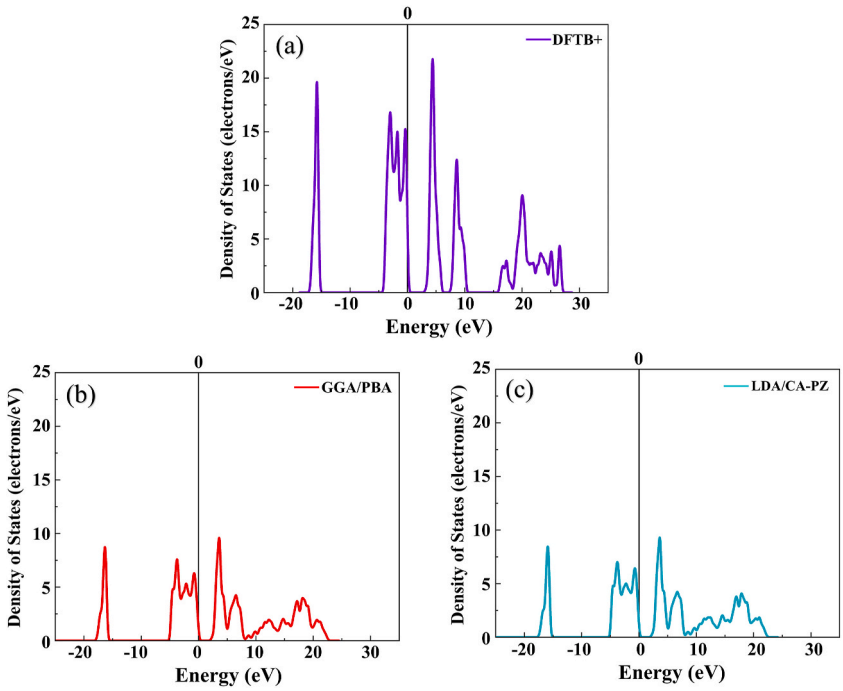

Fig. 5. Total density of states calculated by (a) DFTB+, (b) GGA/PBE, and (c) LDA/CA-PZ functional.

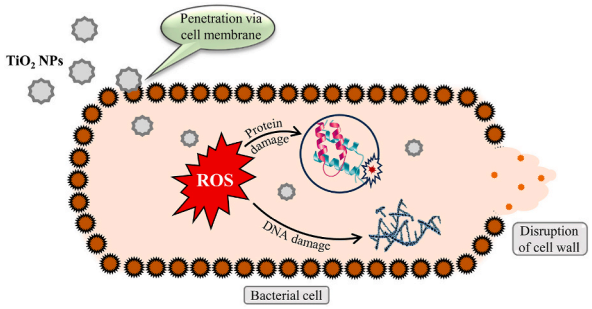

Fig. 6. Antibacterial activity mechanism of TiO_2 NPs.

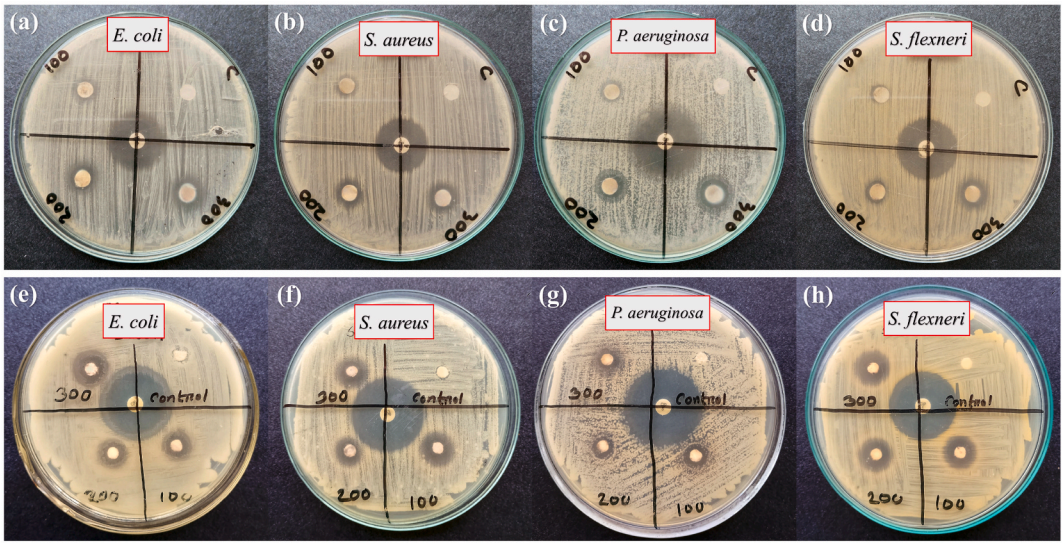

Fig. 7. Antibacterial activity of (a–d) TSol and (e–h) TBio NPs against *E. coli*, *S. aureus*, *P. aeruginosa*, and *S. flexneri* bacteria.

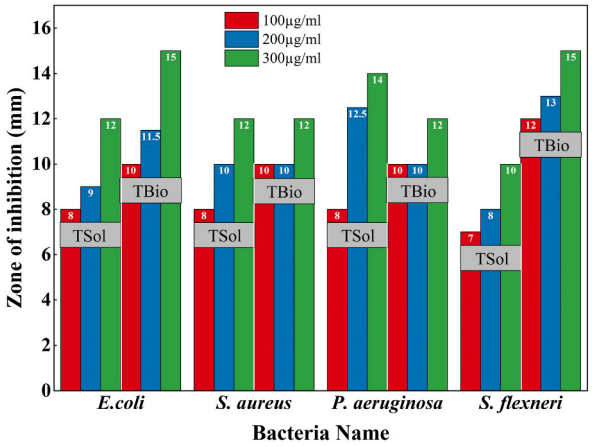

Fig. 8. Histogram of Zone of Inhibition of TSol and TBio NPs against *E. coli*, *S. aureus*, *P. aeruginosa*, and *S. flexneri* bacteria.

measurements were conducted at room temperature and across a range of frequencies (40 Hz–10 kHz). Fig. 9a, b depicts the frequency dependence of the dielectric constant for the TSol and TBio sample, respectively. The insets of each figure show the corresponding loss tangent values. As observed in Fig. 9a, the TSol sample exhibits the highest dielectric permittivity, reaching a value of 27.80 at 1 kHz. This value is accompanied by a tanδ of 0.37 at the same frequency. In comparison, the TBio sample demonstrates a lower dielectric

constant of 19.48 at 1 kHz, with a higher dielectric loss of 0.69 (Fig. 9b).

As shown in Fig. 9a and b, the ε' for both TSol and TBio sample exhibits a characteristic frequency dependence. At lower frequencies, both samples exhibit high ε' values that decrease with increasing frequency. The dielectric constant is fairly remaining constant in the high-frequency region. The high ε' at low frequency is likely due to the combined effect of multiple polarization mechanisms within the material [52,53]. At low frequencies, all four main types (electronic, ionic, orientational, and space-charge) can contribute, with space-charge polarization likely dominating and leading to the initial rise in ε' [54,55]. However, as the frequency increases, these polarization mechanisms become less efficient. They can no longer respond as effectively to the rapidly changing electric field, resulting in a decrease in the overall dielectric constant observed at higher frequencies [56].

The inset of Fig. 9a, b reveals the dependence of tanδ on frequency. Both TSol and TBio samples exhibit a high tanδ at lower frequencies (40 Hz), likely due to the space-charge polarization mechanisms contributing to both dielectric constant and loss [57]. As frequency increases, tanδ decreases gradually, reaching a frequency-independent region above 3 kHz for TBio. This low tanδ value at high frequencies for TBio could be attributed to the nanomaterial's purity, as a purer material with greater crystallinity tends to have a more ordered structure with fewer defects [58]. Notably, the absence of any dielectric loss peak for TBio at higher frequencies indicates its potential suitability for high-frequency optoelectronic applications [59]. In contrast, the TSol sample exhibits a more complex behavior with a second increase in tanδ at higher frequencies, suggesting a possible double relaxation process [60]. However, despite this additional relaxation, the TSol NPs possess a lower tanδ value compared to TBio at 1 kHz.

3.5.1. *Computational analysis of the dielectric properties*

For analyzing the dielectric properties of the TSol and TBio samples in this computational study, we compared them with experimental results for the dielectric function (ϵ (ω)). A key aspect of calculating the complex dielectric function involves using Eqn. (7).

$$\epsilon(\omega) = \epsilon_1(\omega) + i\epsilon_2(\omega) \tag{7}$$

This dielectric function describes the electronic response of the material for the interaction with the electromagnetic wave [61]. The real part (Fig. 10a and b) of the dielectric function is $\epsilon_1(\omega)$, and it can be obtained through Kramers-Kronig relations which relates the real and imaginary part of dielectric function to maintain causality and consistency of optical response of the system. This makes it possible to establish the characteristics of the material used when exposed to different intensities of electromagnetic waves and come up with the theoretical background of the results observed in the experiments.

In the experimental findings, a high dielectric constant at low frequencies shows strong effects of polarization, while as the frequency increases, the polarization effect reduces, as polarization mechanisms are less effective at high frequencies. The same can be observed in the present computational study, where trends occurring below 10 eV coupled with marked peaks represent enhanced dielectric response above this energy limit while beyond which (ϵ_1) tends to reduce gradually. On this basis, it is concluded that, at higher energies (corresponding to the higher frequencies), the material's capacity to the weak polarization decreases, which correlates with the decrease of value (ϵ') observed in the experiment. A comparison between the theoretical estimates and the simulation results shows a good agreement where it emphasizes the strong polarization effects at low frequency or energy range and declines with an increase in frequency or energy. This high dielectric response at lower frequencies as observed in both approaches supports the authenticity of the material's behavior across the different approaches.

4. Conclusions

In conclusion, this study successfully synthesized TiO_2 NPs by sol-gel method and environmentally friendly biosynthesis technique using *Allium sativum* peel extract. Comprehensive analysis through DFTB+, DFT calculations, and experimental techniques provided a

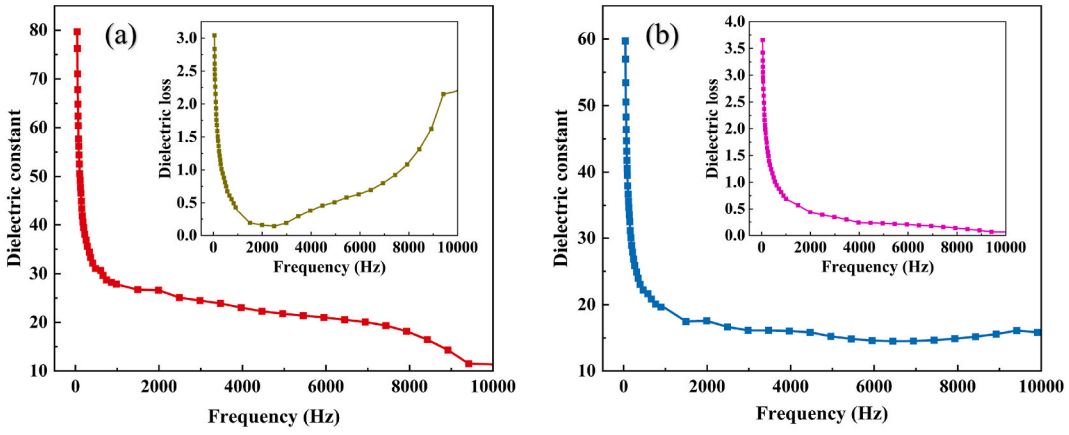

Fig. 9. Frequency dependence of the dielectric behavior for the (a) TSol and (b) TBio sample.

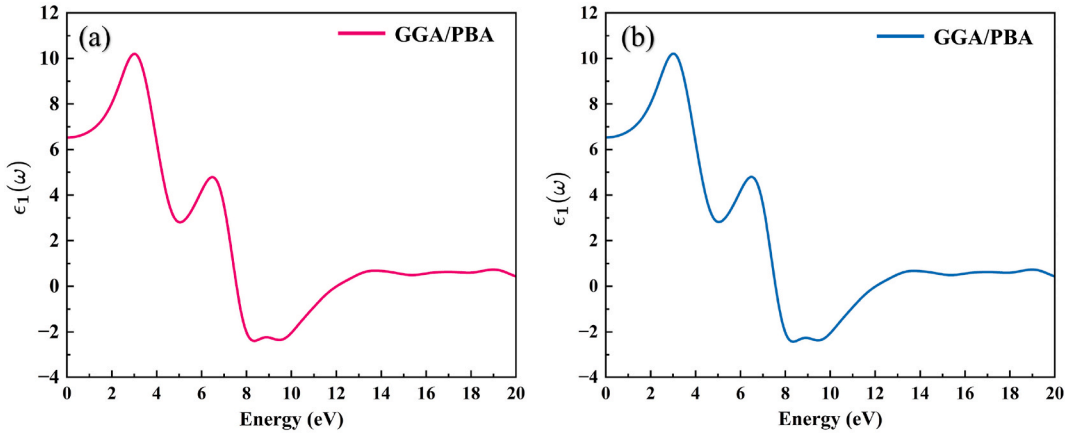

Fig. 10. Calculated real part of the dielectric function ($\epsilon_1(\omega)$) vs energy graph for the (a) TSol and (b) TBio sample.

detailed understanding of the electronic-property relationships of TiO_2 NPs. Notably, the biosynthesized nanoparticles exhibited smaller particle sizes compared to the sol-gel variant. Additionally, the biosynthesized nanoparticles displayed a redshift in their optical absorption and a lower band gap energy of 3.02 eV. Furthermore, the biosynthesized nanoparticles exhibited superior antibacterial activity, with zones of inhibition measuring 15 mm for both *E. coli* and *Shigella flexneri*, outperforming the sol-gel synthesized nanoparticles, which showed maximum inhibition of 14 mm for *P. aeruginosa*. However, the sol-gel variant exhibited a higher dielectric permittivity of 27.80 at 1 kHz, while maintaining a reduced dielectric loss of 0.37. These findings highlight the effectiveness of synthesis method selection in controlling the properties of TiO_2 NPs for diverse applications in optoelectronics, dielectrics, and antibacterial materials.

CRediT authorship contribution statement

Abdullah Al Moyeen: Writing – original draft, Methodology, Formal analysis, Conceptualization, Project administration. **Raiyana Mashfiqua Mahmud:** Writing – original draft, Visualization, Formal analysis. **Durjoy Datta Mazumder:** Writing – original draft, Software. **Sondip Ghosh:** Investigation, Data curation. **Orchi Datta:** Investigation, Data curation. **Anik Molla:** Writing – review & editing, Resources, Data curation. **M. Esmotara Begum:** Writing – review & editing, Validation, Supervision.

Declaration of competing interest

The authors declare that they have no known competing financial interests or personal relationships that could have appeared to influence the work reported in this article.

Acknowledgments

The authors sincerely acknowledge the Department of Glass & Ceramic Engineering, RUET for facilitating this research by providing access to the laboratory facilities.

References

[1] J.M. Romo-Herrera, M. Terrones, H. Terrones, S. Dag, V. Meunier, Covalent 2D and 3D networks from 1D nanostructures: designing new materials, Nano Lett. 7 (2007) 570–576, https://doi.org/10.1021/nl0622202.
[2] C.B. Ng, L.S. Schadler, R.W. Siegel, Synthesis and mechanical properties of TiO2-epoxy nanocomposites, Nanostruct. Mater. 12 (1999) 507–510, https://doi.org/10.1016/S0965-9773(99)00170-1.
[3] G. Nabi, Qurat-ul-Aain, N.R. Khalid, M.B. Tahir, M. Rafique, M. Rizwan, et al., A review on novel eco-friendly green approach to synthesis TiO2 nanoparticles using different extracts, J. Inorg. Organomet. Polym. Mater. 28 (2018) 1552–1564, https://doi.org/10.1007/s10904-018-0812-0.
[4] R. Mohan, J. Drbohlavova, J. Hubalek, Water-dispersible TiO2 nanoparticles via a biphasic solvothermal reaction method, Nanoscale Res. Lett. 8 (2013) 503, https://doi.org/10.1186/1556-276X-8-503.
[5] C.Y. Huang, P. Selvaraj, G. Senguttuvan, C.J. Hsu, Electro-optical and dielectric properties of TiO2 nanoparticles in nematic liquid crystals with high dielectric anisotropy, J. Mol. Liq. 286 (2019) 110902, https://doi.org/10.1016/j.molliq.2019.110902.
[6] L.G. Devi, N. Kottam, B.N. Murthy, S.G. Kumar, Enhanced photocatalytic activity of transition metal ions Mn2+, Ni2+ and Zn2+ doped polycrystalline titania for the degradation of Aniline Blue under UV/solar light, J. Mol. Catal. Chem. 328 (2010) 44–52, https://doi.org/10.1016/j.molcata.2010.05.021.
[7] M.Z. Iqbal, S. Khan, Progress in the performance of dye sensitized solar cells by incorporating cost effective counter electrodes, Sol. Energy 160 (2018) 130–152, https://doi.org/10.1016/j.solener.2017.11.060.
[8] B. Xu, H.Y. Sohn, Y. Mohassab, Y. Lan, Structures, preparation and applications of titanium suboxides, RSC Adv. 6 (2016) 79706–79722, https://doi.org/10.1039/C6RA14507H.
[9] M. Mhadhbi, H. Abderazzak, B. Avar, Synthesis and Properties of Titanium Dioxide Nanoparticles. Updates on Titanium Dioxide, IntechOpen, 2023, https://doi.org/10.5772/intechopen.111577.

[10] P. Raveendran, J. Fu, S.L. Wallen, Completely "green" synthesis and stabilization of metal nanoparticles, J. Am. Chem. Soc. 125 (2003) 13940–13941, https://doi.org/10.1021/ja029267j.

[11] K.N. Thakkar, S.S. Mhatre, R.Y. Parikh, Biological synthesis of metallic nanoparticles, Nanomedicine 6 (2010) 257–262, https://doi.org/10.1016/j.nano.2009.07.002.

[12] A. Castro-Beltrán, P.A. Luque, H.E. Garrafa-Gálvez, R.A. Vargas-Ortiz, A. Hurtado-Macías, A. Olivas, et al., Titanium butoxide molar ratio effect in the TiO2 nanoparticles size and methylene blue degradation, Optik 157 (2018) 890–894, https://doi.org/10.1016/j.ijleo.2017.11.185.

[13] S. Musić, M. Gotić, M. Ivanda, S. Popović, A. Turković, R. Trojko, et al., Chemical and micro structural properties of TiO2 synthesized by sol-gel procedure, Mater. Sci. Eng., B 47 (1997) 33–40, https://doi.org/10.1016/S0921-5107(96)02041-7.

[14] X. Chen, S.S. Mao, Titanium dioxide nanomaterials: synthesis, properties, modifications, and applications, Chem. Rev. 107 (2007) 2891–2959, https://doi.org/10.1021/cr0500535.

[15] A. Ansari, V.U. Siddiqui, W.U. Rehman, MdK. Akram, W.A. Siddiqi, A.M. Alosaimi, et al., Green synthesis of TiO2 nanoparticles using Acorus calamus leaf extract and evaluating its photocatalytic and in vitro antimicrobial activity, Catalysts 12 (2022) 181, https://doi.org/10.3390/catal12020181.

[16] R.S. Dubey, K.V. Krishnamurthy, S. Singh, Experimental studies of TiO2 nanoparticles synthesized by sol-gel and solvothermal routes for DSSCs application, Results Phys. 14 (2019) 102390, https://doi.org/10.1016/j.rinp.2019.102390.

[17] M. Aravind, M. Amalanathan, M.S.M. Mary, Synthesis of TiO2 nanoparticles by chemical and green synthesis methods and their multifaceted properties, SN Appl. Sci. 3 (2021) 409, https://doi.org/10.1007/s42452-021-04281-5.

[18] G. Nabi, Q.-U.- Ain, M.B. Tahir, K. Nadeem Riaz, T. Iqbal, M. Rafique, et al., Green synthesis of TiO $_2$ nanoparticles using lemon peel extract: their optical and photocatalytic properties, Int. J. Environ. Anal. Chem. 102 (2022) 434–442, https://doi.org/10.1080/03067319.2020.1722816.

[19] K.S. Saranya, V. Vellora Thekkae Padil, C. Senan, R. Pilankatta, K. Saranya, B. George, et al., Green synthesis of high temperature stable anatase titanium dioxide nanoparticles using gum kondagogu: characterization and solar driven photocatalytic degradation of organic dye, Nanomaterials 8 (2018) 1002, https://doi.org/10.3390/nano8121002.

[20] W. Buraso, V. Lachom, P. Siriya, P. Laokul, Synthesis of TiO $_2$ nanoparticles via a simple precipitation method and photocatalytic performance, Mater. Res. Express 5 (2018) 115003, https://doi.org/10.1088/2053-1591/aadbf0.

[21] A. Ansari, V.U. Siddiqui, W.U. Rehman, MdK. Akram, W.A. Siddiqi, A.M. Alosaimi, et al., Green synthesis of TiO2 nanoparticles using Acorus calamus leaf extract and evaluating its photocatalytic and in vitro antimicrobial activity, Catalysts 12 (2022) 181, https://doi.org/10.3390/catal12020181.

[22] G. Nabi, A. Majid, A. Riaz, T. Alharbi, M. Arshad Kamran, M. Al-Habardi, Green synthesis of spherical TiO2 nanoparticles using Citrus Limetta extract: excellent photocatalytic water decontamination agent for RhB dye, Inorg. Chem. Commun. 129 (2021) 108618, https://doi.org/10.1016/j.inoche.2021.108618.

[23] R.S. Dubey, K.V. Krishnamurthy, S. Singh, Experimental studies of TiO2 nanoparticles synthesized by sol-gel and solvothermal routes for DSSCs application, Results Phys. 14 (2019) 102390, https://doi.org/10.1016/j.rinp.2019.102390.

[24] M. Marycleopha, B. Yaou Balarabe, I. Adjama, H. Moussa, H. Anandaram, M.W. Abdoul Razak, Anhydrous sol-gel synthesis of TiO2 nanoparticles: evaluating their impact on protein interactions in biological systems, Journal of Trace Elements and Minerals 7 (2024) 100114, https://doi.org/10.1016/j.jtemin.2023.100114.

[25] Z. Alhalili, M. Smiri, The influence of the calcination time on synthesis of nanomaterials with small size, high crystalline nature and photocatalytic activity in the TiO2 nanoparticles calcined at 500 °C, Crystals 12 (2022) 1629, https://doi.org/10.3390/cryst12111629.

[26] J. Yan, G. Wu, N. Guan, L. Li, Z. Li, X. Cao, Understanding the effect of surface/bulk defects on the photocatalytic activity of TiO2: anatase versus rutile, Phys. Chem. Chem. Phys. 15 (2013) 10978, https://doi.org/10.1039/c3cp50927c.

[27] A. Liza Kretzschmar, M. Manefield, The role of lipids in activated sludge floc formation, AIMS Environ Sci 2 (2015) 122–133, https://doi.org/10.3934/environsci.2015.2.122.

[28] S. Iravani, Green synthesis of metal nanoparticles using plants, Green Chem. 13 (2011) 2638, https://doi.org/10.1039/c1gc15386b.

[29] L.K. Ruddaraju, S.V.N. Pammi, G sankar Guntuku, V.S. Padavala, V.R.M. Kolapalli, A review on anti-bacterials to combat resistance: from ancient era of plants and metals to present and future perspectives of green nano technological combinations, Asian J. Pharm. Sci. 15 (2020) 42–59, https://doi.org/10.1016/j.ajps.2019.03.002.

[30] S.P. Goutam, G. Saxena, V. Singh, A.K. Yadav, R.N. Bharagava, K.B. Thapa, Green synthesis of TiO2 nanoparticles using leaf extract of Jatropha curcas L. for photocatalytic degradation of tannery wastewater, Chem. Eng. J. 336 (2018) 386–396, https://doi.org/10.1016/j.cej.2017.12.029.

[31] I.Y. Hernández-Montesinos, D.F. Carreón-Delgado, E. Ocaranza-Sánchez, C.E. Ochoa-Velasco, Á. Suárez-Jacobo, C. Ramírez-López, Garlic (*Allium sativum*) peel extracts and their potential as antioxidant and antimicrobial agents for food applications: influence of pretreatment and extraction solvent, Int. J. Food Sci. Technol. 58 (2023) 6794–6805, https://doi.org/10.1111/ijfs.16652.

[32] E. Subroto, Y. Cahyana, Mahani Tensiska, F. Filianty, E. Lembong, et al., Bioactive compounds in garlic (Allium sativum L.) as a source of antioxidants and its potential to improve the immune system: a review, Food Res. 5 (2021) 1–11, https://doi.org/10.26656/fr.2017.5(6).042.

[33] P. Makkar, N.N. Ghosh, A review on the use of DFT for the prediction of the properties of nanomaterials, RSC Adv. 11 (2021) 27897–27924, https://doi.org/10.1039/D1RA04876G.

[34] M. Gaus, Q. Cui, M. Elstner, Density functional tight binding: application to organic and biological molecules, WIREs Computational Molecular Science 4 (2014) 49–61, https://doi.org/10.1002/wcms.1156.

[35] M. Elstner, G. Seifert, Density functional tight binding, Phil. Trans. Math. Phys. Eng. Sci. 372 (2014) 20120483, https://doi.org/10.1098/rsta.2012.0483.

[36] A.L. Patterson, The scherrer formula for X-ray particle size determination, Phys. Rev. 56 (1939) 978–982, https://doi.org/10.1103/PhysRev.56.978.

[37] H. Kaur, S. Kaur, J. Singh, M. Rawat, S. Kumar, Expanding horizon: green synthesis of TiO $_2$ nanoparticles using Carica papaya leaves for photocatalysis application, Mater. Res. Express 6 (2019) 095034, https://doi.org/10.1088/2053-1591/ab2ec5.

[38] N.K. Sethy, Z. Arif, P.K. Mishra, P. Kumar, Green synthesis of TiO2 nanoparticles from Syzygium cumini extract for photo-catalytic removal of lead (Pb) in explosive industrial wastewater, Green Process. Synth. 9 (2020) 171–181, https://doi.org/10.1515/gps-2020-0018.

[39] P. Makuła, M. Pacia, W. Macyk, How to correctly determine the band gap energy of modified semiconductor photocatalysts based on UV–vis spectra, J. Phys. Chem. Lett. 9 (2018) 6814–6817, https://doi.org/10.1021/acs.jpclett.8b02892.

[40] R. Zedek, H. Djedjiga, M. Megherbi, M.S. Belkaid, E. Ntsoenzok, Effects of slight Fe (III)-doping on structural and optical properties of TiO2 nanoparticles, J. Sol. Gel Sci. Technol. 100 (2021) 44–54, https://doi.org/10.1007/s10971-021-05602-1.

[41] M.M. Ali, MdJ. Haque, M.H. Kabir, M.A. Kaiyum, M.S. Rahman, Nano synthesis of ZnO–TiO2 composites by sol-gel method and evaluation of their antibacterial, optical and photocatalytic activities, Results in Materials 11 (2021) 100199, https://doi.org/10.1016/j.rinma.2021.100199.

[42] X. Pan, M.-Q. Yang, X. Fu, N. Zhang, Y.-J. Xu, Defective TiO2 with oxygen vacancies: synthesis, properties and photocatalytic applications, Nanoscale 5 (2013) 3601, https://doi.org/10.1039/c3nr00476g.

[43] X. Liu, S. Gao, H. Xu, Z. Lou, W. Wang, B. Huang, et al., Green synthetic approach for Ti3+ self-doped TiO2−x nanoparticles with efficient visible light photocatalytic activity, Nanoscale 5 (2013) 1870, https://doi.org/10.1039/c2nr33563h.

[44] M.M. Khan, S.A. Ansari, D. Pradhan, M.O. Ansari, D.H. Han, J. Lee, et al., Band gap engineered TiO $_2$ nanoparticles for visible light induced photoelectrochemical and photocatalytic studies, J. Mater. Chem. A 2 (2014) 637–644, https://doi.org/10.1039/C3TA14052K.

[45] T.P. Dasari, K. Pathakoti, H.-M. Hwang, Determination of the mechanism of photoinduced toxicity of selected metal oxide nanoparticles (ZnO, CuO, Co3O4 and TiO2) to E. coli bacteria, J. Environ. Sci. 25 (2013) 882–888, https://doi.org/10.1016/S1001-0742(12)60152-1.

[46] K. Sunada, T. Watanabe, K. Hashimoto, Studies on photokilling of bacteria on TiO2 thin film, J. Photochem. Photobiol. Chem. 156 (2003) 227–233, https://doi.org/10.1016/S1010-6030(02)00434-3.

[47] B. Pant, M. Park, S.-J. Park, Recent advances in TiO2 films prepared by sol-gel methods for photocatalytic degradation of organic pollutants and antibacterial activities, Coatings 9 (2019) 613, https://doi.org/10.3390/coatings9100613.

[48] B. Pant, H.R. Pant, D.R. Pandeya, G. Panthi, K.T. Nam, S.T. Hong, et al., Characterization and antibacterial properties of Ag NPs loaded nylon-6 nanocomposite prepared by one-step electrospinning process, Colloids Surf. A Physicochem. Eng. Asp. 395 (2012) 94–99, https://doi.org/10.1016/j.colsurfa.2011.12.011.

[49] J. Hou, L. Wang, C. Wang, S. Zhang, H. Liu, S. Li, et al., Toxicity and mechanisms of action of titanium dioxide nanoparticles in living organisms, J. Environ. Sci. 75 (2019) 40–53, https://doi.org/10.1016/j.jes.2018.06.010.
[50] K.R. Raghupathi, R.T. Koodali, A.C. Manna, Size-dependent bacterial growth inhibition and mechanism of antibacterial activity of zinc oxide nanoparticles, Langmuir 27 (2011) 4020–4028, https://doi.org/10.1021/la104825u.
[51] J.-Y. Zhang, X.-Y. Wang, M. Xiao, L. Qu, X. Peng, Lattice contraction in free-standing CdSe nanocrystals, Appl. Phys. Lett. 81 (2002) 2076–2078, https://doi.org/10.1063/1.1507613.
[52] A.K. Abdul Gafoor, J. Thomas, M.M. Musthafa, P.P. Pradyumnan, Effects of Sm3+ doping on dielectric properties of anatase TiO2 nanoparticles synthesized by a low-temperature hydrothermal method, J. Electron. Mater. 40 (2011) 2152–2158, https://doi.org/10.1007/s11664-011-1707-9.
[53] A.K. Abdul Gafoor, M.M. Musthafa, K. Pradeep Kumar, P.P. Pradyumnan, Effect of Ag doping on structural, electrical and dielectric properties of TiO2 nanoparticles synthesized by a low temperature hydrothermal method, J. Mater. Sci. Mater. Electron. 23 (2012) 2011–2016, https://doi.org/10.1007/s10854-012-0695-8.
[54] X. Wang, B. Zhang, L. Xu, X. Wang, Y. Hu, G. Shen, et al., Dielectric properties of Y and Nb co-doped TiO2 ceramics, Sci. Rep. 7 (2017) 8517, https://doi.org/10.1038/s41598-017-09141-0.
[55] A.K. Yadav, C. Gautam, Dielectric behavior of perovskite glass ceramics, J. Mater. Sci. Mater. Electron. 25 (2014) 5165–5187, https://doi.org/10.1007/s10854-014-2311-6.
[56] S. Chao, V. Petrovsky, F. Dogan, Effects of sintering temperature on the microstructure and dielectric properties of titanium dioxide ceramics, J. Mater. Sci. 45 (2010) 6685–6693, https://doi.org/10.1007/s10853-010-4761-4.
[57] B. Ghosh, R.M. Tamayo Calderón, R. Espinoza-González, S.A. Hevia, Enhanced dielectric properties of PVDF/CaCu 3 Ti 4 O 12 :Ag composite films, Mater. Chem. Phys. 196 (2017) 302–309, https://doi.org/10.1016/j.matchemphys.2017.05.009.
[58] P. Saravanan, M. Ganapathy, A. Charles, S. Tamilselvan, R. Jeyasekaran, M. Vimalan, Electrical properties of green synthesized TiO2 nanoparticles. Pelagia Research Library, Adv. Appl. Sci. Res. 7 (2016) 158–168.
[59] R. Narzary, B. Dey, S.N. Rout, A. Mondal, G. Bouzerar, M. Kar, et al., Influence of K/Mg co-doping in tuning room temperature d0 ferromagnetism, optical and transport properties of ZnO compounds for spintronics applications, J. Alloys Compd. 934 (2023) 167874, https://doi.org/10.1016/j.jallcom.2022.167874.
[60] X. Zhao, L. Chen, X. Zhang, P. Liu, C.-L. Xu, Z.-Y. Hou, et al., The abnormal multiple dielectric relaxation responses of Al3+ and Nb5+ co-doped rutile TiO2 ceramics, J. Alloys Compd. 860 (2021) 157891, https://doi.org/10.1016/j.jallcom.2020.157891.
[61] A.H. Reshak, S.A. Khan, Z.A. Alahmed, Investigation of electronic structure and optical properties of MgAl2O4: DFT approach, Opt. Mater. 37 (2014) 322–326, https://doi.org/10.1016/j.optmat.2014.06.017.